Int. J. Heat Mass Transfer. Vol. 35, No. 2, pp. 469–480, 1992
Printed in Great Britain

0017–9310/92 $5.00+0.00

Funicular and evaporative-front regimes in convective drying of granular beds

J. A. ROGERS† and M. KAVIANY
Department of Mechanical Engineering and Applied Mechanics, The University of Michigan, Ann Arbor, MI 48109, U.S.A.

(*Received* 10 *July* 1990 *and in final form* 12 *February* 1991)

Abstract—Convective heating of an initially partially saturated packed bed and the consequent surface and internal evaporation of the liquid is considered for cases where the temperature everywhere in the bed is below the saturation temperature at the local total pressure. In the first period where the liquid phase is continuous (funicular regime), the effect of surface tension nonuniformity on the liquid and gas phase flows is examined. The critical time (the time at which the surface saturation becomes equal to the immobile saturation) is found from the integration of the conservation equations. The effect of the absolute permeability heterogeneities on this critical time is examined, and it is shown that for normal distributions in porosity, the critical time increases over that for homogeneous permeabilities. The mass transfer rate during the evaporative front regime is also predicted by treating both the dry and the wet regions and the moving interface. An experiment is performed in which a 0.10 mm glass spheres–ethanol bed is convectively dried, and good agreement is found between the predicted and measured mass transfer rates, critical times, and surface temperatures.

1. INTRODUCTION

ONE AREA of study associated with phase change in porous media is that of heat addition to an initially highly liquid saturated medium (saturation is the fraction of void space occupied by the liquid phase). Here we consider those partially saturated porous media with solid matrices that do not absorb water, i.e. non-hygroscopic porous media. In these matrices, the liquid moves through the pores and not within the solid phase. The liquid can also be adsorbed to the surface of the solid matrix (capillary condensation [1]). This adsorption, which is due to the van der Waals' dispersive forces, is significant when the pores are very small (smaller than 1 μm). We will not address surface adsorption/desorption here and will only consider pore sizes larger than 1 μm. When one of the surfaces is permeable and heat is added through this surface, and when, in addition, the temperature of this partially saturated porous medium is no higher than the boiling point anywhere within the medium, i.e. $T(x) < T_s(p_g)$, then this transient liquid removal from the porous medium will have two distinct regimes. In the first regime, the liquid phase is connected throughout the medium and the liquid and its vapor are in thermodynamic equilibrium (the equilibrium state is influenced by the meniscus curvature as described by Defay and Prigogine [2]). This regime is called the funicular regime because of the early misconceptions about phase distributions of two-phase flow in porous media. According to these misconceptions, both phases flowed simultaneously through channels with the gas moving in the inner core and the liquid in an annulus and the gas phase flowed inside and the solid channel walls (not necessarily constant area channels) on the outside. Flow visualizations have shown that the gas and liquid phases flow through their own network of channels [3]. In this regime, the liquid flows due to the gradient in the capillary pressure, and gravity can assist or oppose the flow. In addition, the presence of a temperature gradient within the medium and the consequent existence of a surface tension gradient moves the liquid away from the heated surface (opposing the capillary effect). Thus, capillarity, gravity, and thermo-capillarity are the most significant forces governing the liquid motion. As the liquid flows out of the medium, the local saturation, throughout, decreases with the saturation at the heated permeable surface decreasing the fastest (because the flow is towards the lowest saturation and also the resistance to liquid flow increases with decrease in saturation thus requiring large saturation gradients). The end of the funicular regime is marked with the surface saturation dropping to the irreducible saturation s_{ir}. The time at which this occurs is called the *critical time* t_c [4]. For a short period after t_c, the heated surface will be intermittently dry which is associated with a decrease in the drying rate. After this intermittent surface-drying period, the moving interface regime begins. The surface becomes completely dry, the surface temperature increases rapidly, and the heat transferred to the porous medium results in penetration of the evaporation front (a moving interface) into the medium. Figure 1 shows the two regimes and gives the saturation and temperature

† Present address: Babcock and Wilcox, Heat Transfer and Fluid Mechanics, Alliance, OH 44061, U.S.A.

NOMENCLATURE

A	area [m^2]
Bo	Bond number, $g\rho_l R^2/\sigma$
C	$(\rho c_p)_s/(\rho c_p)_l$
c_p	specific heat capacity [$J\,kg^{-1}\,K^{-1}$]
d	diameter of sphere [m]
D	binary mass diffusion coefficient [$m^2\,s^{-1}$]
D_h	total thermal diffusion coefficient [$m^2\,s^{-1}$]
D_m	total mass diffusion coefficient [$m^2\,s^{-1}$]
g	gravitational constant [$m\,s^{-2}$]
h	heat transfer coefficient [$W\,m^{-2}\,K^{-1}$]
h_m	mass transfer coefficient [$m\,s^{-1}$]
i_{lg}	specific heat of vaporization [$J\,kg^{-1}$]
k	thermal conductivity [$W\,m^{-1}\,K^{-1}$]
K	permeability [m^2]
Le	Lewis number, α_g/D
$\dot{m}$	mass flux [$kg\,m^{-2}\,s^{-1}$]
M	molecular weight [kg (kg-mol)$^{-1}$]
$\dot{n}$	volumetric evaporation rate [$kg\,m^{-3}\,s^{-1}$]
p	pressure [Pa]
Pe	Peclet number, uR/α or uB/D
q	heat flux [$W\,m^{-2}$]
R	radius [m]
Re	Reynolds number, uR/v
R_g	universal gas constant, 8.3144 kJ kg^{-1} mol^{-1} K^{-1}
s	saturation (wetting-phase)
S	reduced saturation $(s-s_{ir})/(1-s_{ir}-s_{irg})$
u	velocity [$m\,s^{-1}$]
V	volume [m^3]
t	time [s]
t_c	critical time [s]
T	temperature [K]
x	coordinate axis [m]
x_i	interfacial location [m].

Greek symbols

α	thermal diffusivity [$m^2\,s^{-1}$]
ε	porosity
μ	dynamic viscosity [Pa s]
v	kinematic viscosity [$m^2\,s^{-1}$]
ρ	density [$kg\,m^{-3}$]
σ	surface tension [Pa m]
σ_0	standard deviation.

Superscripts

d	dispersion
$\bar{}$	porosity averaged.

Subscripts

α	ambient
c	condensible, capillary
g	gas
h	heat
i	interface
ir	irreducible
l	liquid
m	mass
n	noncondensible
0	initial
1	at $x = L$.

evolutions during convective heating of the surface. A description similar to that given above is presented by Whitaker and Chou [5] for nonabsorbing solid matrices and by Stanish *et al.* [6] for absorbing (hygroscopic) solid matrices.

In our study, we examine heat addition in these two regimes (funicular and evaporative front) by performing experiments and a one-dimensional, transient analysis. We are able to:

(a) Extend the previous treatment of ref. [4] to include the evaporative–penetration front.

(b) Clarify the relationship between the heat and mass transfer coefficients at the interface of a partially liquid saturated medium and an ambient plain medium and discuss the effect of surface saturation on these coefficients.

(c) Discuss the effect of the presence of a surface tension gradient on the liquid flow and give the appropriate momentum equation.

(d) Examine the role of porosity heterogeneity and its effect on the capillary flow and on the critical time.

In the experiments a packed bed of glass spheres of 0.10 mm diameter is initially partially saturated by ethanol and is at nearly uniform temperature. Then heated air is blown over its upper permeable surface. In the analysis, the two-phase flow and heat transfer in porous media are addressed using semi-empirical transport and constitutive equations. It should be mentioned that non-intensive drying (i.e. $T(x) < T_s(p_g)$) is not a problem in which a critical evaluation of the semi-empirical, two-phase flow momentum equations can be made. These problems are controlled by the external heat supply during the funicular regime and by heat and mass diffusion in the dry zone during the evaporative front penetration. However, for these problems, a proper description of porous/plain media interfacial heat and mass transfer coefficients is essential.

2. EXPERIMENT

The bed of 0.10 mm spherical glass particles (porosity $\varepsilon = 0.40$) is placed so that its permeable surface is flush with the lower surface of a wind tunnel. The tunnel and the walls of the bed are made of Plexiglas. The air drawn into the tunnel is heated with a 1.5 kW heater and placed upstream of the bed.

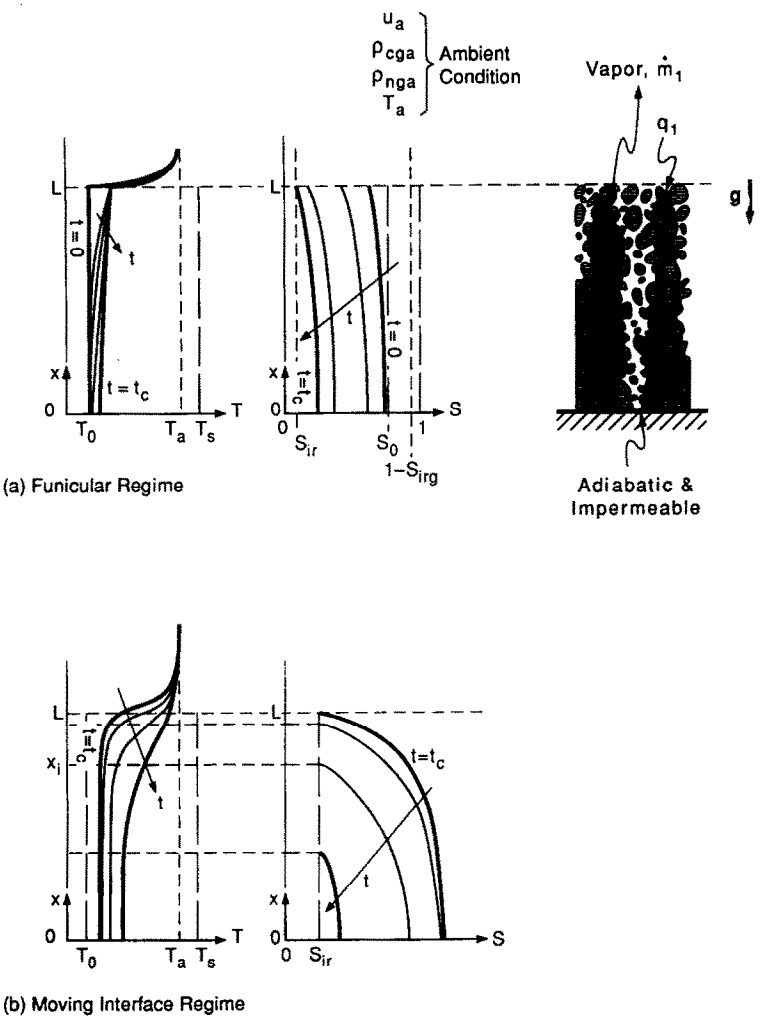

FIG. 1. A schematic of the problem considered and the distribution of saturation and temperature during: (a) the funicular regime; (b) the evaporative, moving front regime.

Downstream of this heater is a passive mixer used for temperature uniformity and a polyurethane foam block used for velocity uniformity. The velocity field over the bed is measured with a precalibrated hot wire, and the velocity outside the boundary layer is found to be nearly uniform. The packed bed is 15 × 15 cm in cross section and has a depth of 25.4 mm. The temperature of the air and at several locations within the bed is measured.

The bed is initially flooded with ethanol. This results in a saturation distribution $s_0(x)$ and a temperature distribution $T(x)$, where both are nonuniform. The initial saturation distribution is determined by the irreducible, nonwetting phase saturation s_{irg} and the local balance between capillarity and gravity. The initial temperature nonuniformity is due to unavoidable evaporation prior to the start of the convective heating. The heat for this evaporation (both surface and internal) is supplied mostly from the bed, resulting in a decrease in the bed temperature, mostly near the bed surface.

The bed is periodically (every 1–10 min, depending on the mass transfer rate) lowered and placed on a digital scale for measurement. The blower and heater in the wind tunnel are turned off during this measurement. The accuracy of the scale is 0.01 g, and the accuracy of the thermocouples is ± 0.1°C. An infrared camera is also used to measure the bed surface temperature, and the readings of this and the surface thermocouple are in agreement to within 1°C.

The permeability of the bed is found from the Carman–Kozeny equation (which is proven accurate for randomly arranged spherical particles [4])

$$K = \frac{d^2\varepsilon^3}{180(1-\varepsilon)^2} \tag{1}$$

and is 9.9×10^{-12} m^2.

The heat and mass transfer coefficients for the flooded surface (surface saturation of unity, i.e. $s_1 = 1$) are determined by measuring the mass transfer rate (which is the product of the mass flux $\dot{m}$ and

surface area A) and the difference between the surface and ambient temperatures, i.e.

$$h = \frac{\dot{m} i_{lg}}{T_l - T_a}. \quad (2)$$

The analogy between heat and mass transfer, for fully liquid covered surfaces, can be used if proper account of the properties are made [7], and this gives for the mass transfer coefficient

$$h_m = \frac{h}{(\rho c_p)_{ga} Le^{2/3}}. \quad (3)$$

In the following we report results for an air flow rate which gives $T_a = 55°C$, $h = 18.3\ W\ m^{-2}\ K^{-1}$, and $h_m = 0.10\ m\ s^{-1}$. The density of ethanol in ambient ρ_{cga} is zero.

3. ANALYSIS

3.1. *Funicular regime*

The one-dimensional, transient, two-phase flow (depicted in Fig. 1) is described using the concept of relative permeability and the continuity and momentum equations as given by Whitaker [8], except the shear drag at the interface of the liquid and gaseous phases and the microscopic and macroscopic inertial forces are negligible for this problem. However, the effect of the surface tension gradient can be important, and the formulation of Bear and Bensabat [9] is used. These give

$$\rho_l \varepsilon \frac{\partial s}{\partial t} + \rho_l \frac{\partial u_l}{\partial x} = -\dot{n} \quad (4)$$

$$\varepsilon \frac{\partial \rho_g (1-s)}{\partial t} + \frac{\partial \rho_g u_g}{\partial x} = \dot{n} \quad (5)$$

$$u_l = -\frac{K_l}{\mu_l}\left(\frac{\partial p_l}{\partial x} + \rho_l g\right) + K_{l\Delta\sigma}\frac{\partial \sigma}{\partial x} \quad (6)$$

$$u_g = -\frac{K_g}{\mu_g}\left(\frac{\partial p_g}{\partial x} + \rho_g g\right) + K_{g\Delta\sigma}\frac{\partial \sigma}{\partial x} \quad (7)$$

where u_l and u_g are the superficial velocities (averaged over the entire pore volume). We have treated the liquid phase as incompressible and the gaseous phase is assumed to behave ideally with

$$\rho_{cg} = \frac{p_{cg} M_{cg}}{R_g T}, \quad \rho_{ng} = \frac{p_{ng} M_{ng}}{R_g T}, \quad p_{cg} = p_{cg}(T, p_c)$$

$$\rho_g = \rho_{cg} + \rho_{ng}, \quad p_g = p_{cg} + p_{ng},$$

$$u_g = \frac{\rho_{cg} u_{cg} + \rho_{ng} u_{ng}}{\rho_g} \quad (8)$$

with c standing for condensible and n for noncondensible. The vapor and liquid are in equilibrium, and the effect of curvature on the equilibrium state is included [2]. The local volumetric evaporation rate is $\dot{n}$ [kg m^{-3} s^{-1}]. The species conservation for the noncondensible gas component is treated as a binary mixture (noncondensible and condensible) and is given by

$$\varepsilon \frac{\partial \rho_{ng}(1-s)}{\partial t} + \frac{\partial \rho_{ng} u_g}{\partial x} = \frac{\partial}{\partial x} D_m \rho_g \frac{\partial}{\partial x}\frac{\rho_{ng}}{\rho_g} \quad (9)$$

where

$$D_m = D_{me} + D^d_{ml} + D^d_{mg} \quad (10)$$

where D_{me} is the effective molecular mass diffusion. We can use the results for gas impermeable solid phase for single-phase flows given by Neale and Nader [10]. Assuming that diffusion through the liquid phase is negligible and using a linear relation with saturation, this gives

$$\frac{D_{me}}{D} = \frac{2\varepsilon}{3-\varepsilon}(1-s) \quad (11)$$

where D is the binary mass diffusion in plain media. The mass dispersion coefficient D^d_{ml} for transport of noncondensibles through the liquid phase is negligible and that for the gaseous phase can be approximated by using the result of Koch and Brady [11], along with a linear relation for saturation, i.e.

$$\frac{D^d_{mg}}{D} = \varepsilon\left[0.75 Pe_g + \frac{1}{6}\pi^2(1-\varepsilon) Pe_g \ln Pe_g\right](1-s) \quad (12)$$

$$Pe_g = \frac{u_g R}{D}. \quad (13)$$

Note that D_m appearing in the species conservation equation (9) is the longitudinal component of the total effective mass diffusivity tensor. The velocity of the noncondensible molecules used in equation (9) is given by

$$u_{ng} = u_g - \frac{\rho_g}{\rho_{ng}} D_m \frac{\partial}{\partial x}\frac{\rho_{ng}}{\rho_g}. \quad (14)$$

The energy equation is given by

$$\left[(1-\varepsilon)C + \varepsilon s + \varepsilon(1-s)\frac{(\rho c_p)_{cg} + (\rho c_p)_{ng}}{(\rho c_p)_l}\right]\frac{\partial T}{\partial t} + \left\{u_l + \left[\frac{(\rho c_p)_{cg} + (\rho c_p)_{ng}}{(\rho c_p)_l} u_g\right]\right\}\frac{\partial T}{\partial x} + i_{lg}\dot{n} = \frac{\partial}{\partial x} D_h \frac{\partial T}{\partial x} \quad (15)$$

where D_h is total effective thermal diffusivity

$$D_h = D_{he} + D^d_{hl} + D^d_g \quad (16)$$

and where, again, these are the longitudinal components of the total effective thermal diffusion tensor.

From Somerton *et al.* [12], and Udell and Fitch [13], we have

$$\frac{D_{he}}{\alpha_l} = \frac{k_e(s=0)}{k_l} + s^{1/2}\frac{k_e(s=1) - k_e(s=0)}{k_l} \quad (17)$$

where k_e is the effective thermal conductivity, and its value for the packed beds of spheres saturated fully with liquid ($s = 1$) and gas ($s = 0$) are needed. A convenient and relatively accurate correlation is that given by Krupiczka [14] as

$$\frac{k_c}{k_f} = \left(\frac{k_s}{k_f}\right)^{0.280 - 0.757\log\varepsilon - 0.057\log(k_s/k_f)} \tag{18}$$

where k_f is the liquid or gas thermal conductivity.

The dispersion components of the total effective thermal diffusivity are described in a manner similar to equation (12) using the gas and liquid Peclet numbers (similar to that defined in equation (13)). The liquid phase momentum equation can be written using the capillary pressure $p_c = p_g - p_l$ and making the reasonable assumption that $\sigma = \sigma(T)$ only. Then equation (6) becomes

$$u_l = -\frac{K_l}{\mu_l}\left(\rho_l g + \frac{\partial p_g}{\partial x} - \frac{\partial p_c}{\partial x}\right) + K_{l\Delta\sigma}\frac{\partial\sigma}{\partial T}\frac{\partial T}{\partial x}. \tag{19}$$

We then use the Leverett relation, i.e.

$$p_c = \frac{\sigma}{(K/\varepsilon)^{1/2}}J(s)$$

to find $\partial p_c/\partial s$ and $\partial p_c/\partial T$. This gives

$$\frac{\partial p_c}{\partial x} = \frac{\sigma}{(K/\varepsilon)^{1/2}}\frac{\partial J}{\partial s}\frac{\partial s}{\partial x} + \frac{J}{(K/\varepsilon)^{1/2}}\frac{\partial\sigma}{\partial T}\frac{\partial T}{\partial x}. \tag{20}$$

The thermo-capillary coefficients $K_{l\Delta\sigma}$ and $K_{g\Delta\sigma}$ are functions of the matrix structure, s, σ, wettability, μ_l/μ_g, and the liquid and gas phase distributions in the pores (which are history dependent). A very simple model applicable under restricted conditions, is given by Bear and Bensabat as

$$K_{l\Delta\sigma} = \frac{A_{lg}}{V_l}\frac{1}{1+L_{tl}}\frac{K_l}{\mu_l} \tag{21}$$

$$K_{g\Delta\sigma} = \frac{A_{lg}}{V_g}\frac{1}{1+L_{tg}}\frac{(1-s)\mu_g}{(1-s)\mu_g + s\mu_l}\frac{K_g}{\mu_g} \approx \frac{A_{lg}}{V_g}\frac{1}{L_{tg}}\frac{1-s}{s}\frac{K_g}{\mu_l} \tag{22}$$

where A_{lg}/V_l is the specific liquid–gas surface area, and $1+L_{tl}$ is the tortuosity of the liquid phase. Both of these, as well as their gaseous counterparts, are functions of saturation. Due to the lack of an alternative, we estimate the liquid surface area as being equal to a fraction of the solid surface area (i.e. independent of s). Then, for beds of spherical particles and by allowing for saturation dependencies that satisfy the expected asymptotes, we have

$$\frac{A_{lg}}{V_l} \approx a_1\frac{4\pi R^2}{\left(\frac{\varepsilon}{1-\varepsilon}\right)\frac{4}{3}\pi R^3}(1-s)s = a_1\frac{3(1-\varepsilon)}{\varepsilon R}(1-s)s \tag{23}$$

also

$$\frac{A_{lg}}{V_g} \approx a_1\frac{3(1-\varepsilon)}{\varepsilon R}(1-s)s \tag{24}$$

where a_1 is constant with a magnitude less than unity. We also estimate the tortuosities (the ratio of the actual length a tracer takes in moving through a bed of length L_t to the straight-line path, i.e. L) to be independent of s and equal to $((3-\varepsilon)/2)^{1/2}$.

The phase permeabilities are given as the product of the absolute and relative permeabilities and, including $J(s)$, are already discussed in ref. [4]. Equations (1)–(4) can be combined, and the result is the so-called saturation equation stating the overall mass conservation in terms of the driving forces of the flows. Then, along with equations (12) and (15), they can be solved for the three unknowns s, ρ_{ng}, and T. The required boundary condition at the surface $x = L$ and at the lower, adiabatic, impermeable surface are:

at $x = L$

$$\dot{m}_l = \rho_l u_l + \rho_{cg}u_g - \rho_g D_m\frac{\partial}{\partial x}\frac{\rho_{cg}}{\rho_g} = h_m(\rho_{cg} - \rho_{cga}) \tag{25}$$

$$q_l = \rho_l u_l i_{lg} + (\rho c_p)_l D_h\frac{\partial T}{\partial x} = h(T_a - T) \tag{26}$$

$$p_{cg} + p_{ng} = p_{ga} \tag{27}$$

at $x = 0$

$$\frac{\partial\rho_{cg}}{\partial x} = \frac{\partial\rho_{ng}}{\partial x} = \frac{\partial s}{\partial x} = u_l = u_g = \frac{\partial T}{\partial x} = 0. \tag{28}$$

The initial conditions are approximated here as isothermal. Taking the pressure in the gas phase to be hydrostatic (note that complete displacement of the nonwetting phase is not possible without large applied pressures), the initial saturation distribution $s_0(x)$ is determined from the reduced form of equation (19), i.e.

$$\frac{dp_c(s_0)}{dx} + (\rho_l - \rho_g)g = 0 \tag{29}$$

with a prescribed s_0 at $x = 0$. This value, for example, can be $1 - s_{irg}$. For a completely filled (except for irreducible nonwetting phase saturation) bed, the saturation is uniform and at $1 - s_{irg}$. The irreducible nonwetting and wetting phase saturations s_{irg} and s_{ir} must also be specified.

We now discuss dependence of h and h_m on the surface saturation. It was shown in ref. [15] that using convective drying of partially saturated packed beds of different size spherical particles, for Bond numbers ($Bo = g\rho_l R^2/\sigma$) less than 0.01 and for moderate Reynolds numbers ($Re = u_a R/\nu_a$), the heat and mass transfer coefficients are independent of the surface saturation (during the funicular state). The results of ref. [16] using steady-state, simultaneous heat and mass transfer for two-dimensional, partially liquid covered

surfaces also confirm this phenomenon. Schlünder [17] used a diffusion model to show that for small Bond numbers and when the thickness of the concentration boundary layer is much larger than R, the vapor molecules leaving the liquid patches of the surface diffuse sidewise and cover the dry patches. These molecules then diffuse through the boundary layer (along with other molecules that directly leave the liquid patches and diffuse toward the edge of the boundary layer). As both *Re* and *Bo* tend to zero, the effect of surface saturation on the mass transfer rate diminishes. This is the case for the experiment considered here, as will be evident from the nearly constant evaporation rate in the funicular regime. For large *Bo* and *Re*, the heat transfer through the exposed solid and the substrate has to be included, also the effect of the solid and liquid conductivities, among other parameters, should be considered [16]. Further discussion on various aspects of two-phase flow and heat transfer in porous media can be found in ref. [18].

3.2. *Porosity heterogeneity*

The porosity or the pore size (or particle size) used in the volume-averaged equation is the average value over a representative elementary volume, and in our analysis, we have assumed that this average porosity (or particle size) is uniform throughout the packed bed. We now allow for the porosity (or particle size) to have a distribution in the elementary representative volume with an average value of $\bar{\varepsilon}$. In connection with the one-dimensional problem considered, this porosity heterogeneity in the representative elementary volume causes an alteration in the local capillary pressure. This alteration is a result of imposed lack of lateral capillary pressure gradient. Then at a location x, the liquid saturation of various pore sizes must be such that the capillary pressure for these pores at this location x must be the same. This redistribution of the liquid at location x among the pores favors filling of the smaller pores more than the larger ones (in order to keep the capillary pressure of all these pores at location x the same). We are interested in examining the effect of this porosity heterogeneity on the critical time, as we expect that the smaller the porosity (and permeability) the smaller will be the critical time (because of the extra resistance to the liquid flow and the larger required $\partial s/\partial x$ [4]). In particular, we look for a normal distribution of porosity around $\bar{\varepsilon}$ and examine the effect of this distribution on the critical time.

We choose a Gaussian probability distribution function for porosity, i.e.

$$P(\varepsilon) = \frac{K_t}{(2\pi)^{1/2}\sigma_0} e^{-(\varepsilon-\bar{\varepsilon})/2\sigma_0}. \quad (30)$$

We also specify that $\bar{\varepsilon}-\Delta\varepsilon \leqslant \varepsilon \leqslant \bar{\varepsilon}+\Delta\varepsilon$. In equation (30), K_t is the truncation constant and σ_0 the standard deviation. The J-function used is that found by correlating the data of Leverett [19] for the drainage branch of the capillary pressure–saturation curve. This particular $J(s)$ is given by Udell and Fitch as

$$J(S) = 1.417(1-S) - 2.102(1-S)^2 + 1.266(1-S)^3 \quad (31)$$

where the reduced saturation is

$$S = \frac{s - s_{ir}}{1 - s_{ir} - s_{irg}}. \quad (32)$$

For a given p_c, an implicit equation for S can be written as

$$S = 1 - \frac{p_c}{\sigma[1.417 - 2.102(1-S)^2 + 1.266(1-S)^3]} \times \left[\frac{K(\varepsilon)}{\varepsilon}\right]^{1/2}. \quad (33)$$

The average local saturation is

$$\bar{s} = \int_{\bar{\varepsilon}-\Delta\varepsilon}^{\bar{\varepsilon}+\Delta\varepsilon} sP(\varepsilon)\,d\varepsilon. \quad (34)$$

Other variables such as u_l and u_g are also averaged, e.g.

$$\bar{u}_l = \int_{\bar{\varepsilon}-\Delta\varepsilon}^{\bar{\varepsilon}+\Delta\varepsilon} u_l P(\varepsilon)\,d\varepsilon. \quad (35)$$

Now, the s, T, and ρ_{ng} equations are averaged using the porosity averaging shown above. Then, for a given average saturation $\bar{s}(x)$ found from the solution of these equations, an iterative scheme is executed to find a capillary pressure that satisfies this average saturation. A capillary pressure p_c is guessed and used in equation (33) and $S(\varepsilon)$ is found. Then, the average of this $S(\varepsilon)$ is taken using equations (32) and (34) and compared with the given $\bar{s}$.

The capillary pressure–saturation curve for various porosity distributions can be found by specifying σ_0, $\bar{\varepsilon}$, and $\Delta\varepsilon$. For this, we only iterate on the capillary pressure as outlined above. The results are given in Fig. 2. As was mentioned, the distribution of the

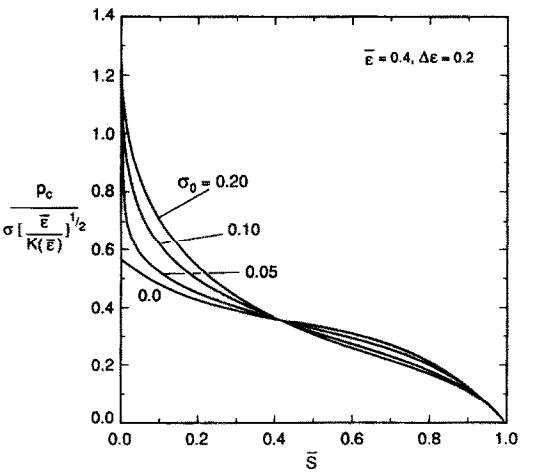

FIG. 2. Effect of porosity heterogeneity on the variation of the capillary pressure with respect to average, reduced saturation $\bar{S}$.

liquid required for capillary pressure uniformity among pores favors filling of the small pores more than the large ones. Therefore, small saturations having a nonzero standard deviation cause an increase in the local capillary pressure. This is evident in Fig. 2. For large saturations, the Gaussian porosity distribution used does not result in a significant change in $p_c(S)$. Therefore, we expect this distribution to become significant only when the local saturations drop significantly, i.e. near the critical time. The largest standard deviation σ_0 used in Fig. 2 is 0.20, but there is an asymptotic behavior for large σ_0 that seems to be approaching the results for $\sigma_0 > 0.20$. The value of $\Delta\varepsilon$ has a more pronounced effect on p_c, and we have limited it to 0.2 for the sake of computational economy and because it is realistic.

Note that we could use the histograms showing the distribution of the particle size (d) instead of the porosity distribution. Both ε and d in turn influence K through relations such as equation (1). Therefore, our discussion of porosity heterogeneity is more general and applies to any heterogeneity in the matrix which causes a heterogeneity in K.

3.3. *Evaporative front regime*

As was mentioned, at $t = t_c$ the surface saturation becomes the immobile saturation s_{ir} and for a short period thereafter, the surface dries out intermittently. After this intermittent period, the addition of heat to the surface results in evaporation in a front that has saturation of s_{ir}. This evaporation front moves inward into the bed as the heat addition proceeds. The temperature of this evaporation is not known a priori, and part of the heat arriving at this front (through the dry region) results in raising the temperature of the wet region. The front position, $x_i(t)$, is primarily determined by the transport of heat and species in the dry region ($x \leqslant x_i$). In convective heating of the beds, in addition to the surface (or film) resistance to heat flow, this dry region also offers resistance to the heat flow (which in general is much larger than the film resistance). The flow of heat through the gas saturated dry region is by axial conduction and against the flow of the condensible gas. The description of the two-phase region is that given in Section 3.1. In the dry region, we use equation (7) for the gas flow with $K_{g\Delta\sigma} = 0$. The gas continuity equation, the species conservation equation, the total effective mass diffusion coefficient, and the energy equation given for two-phase flow, hold except we use $s = 0$ and $\dot{n} = 0$ in the dry region.

Once the surface dries out, the heat transfer from the dry surface will be that of heat transfer from a rough surface with transfer of noncondensibles through the surface pores into the bed, and of the vapor out of the bed. The flow of the gases across the surface influences the heat transfer slightly. However, as was mentioned, the film resistance at the surface is much smaller than the resistance offered in the dry region. For mass transfer, a similar phenomena occurs near the surface, except the mass transfer is only through the pores (gas phase), as heat transfer can occur through the gas and solid phases. Here we choose the same heat and mass transfer coefficients given in Section 2 and, again, assume the validity of the analogy to continue even for the dry surface. The boundary condition for $x = L$, i.e. equations (25)–(27) hold except we have $u_l = 0$. Also, in the dry zone, the vapor is no longer in thermodynamic equilibrium, and, therefore, its temperature is determined by the energy equation and boundary conditions.

At the evaporative front ($x = x_i$), we have

$$\left[(\rho c_p)_l D_h \frac{\partial T}{\partial x}\right]_{x_i^+} = \left[(\rho c_p)_l D_h \frac{\partial T}{\partial x}\right]_{x_i^-} + i_{lg}\rho_{cg}[u_{cg}(x_i^+) - u_{cg}(x_i^-)] \quad (36)$$

$$\rho_{cg}[u_{cg}(x_i^+) - u_{cg}(x_i^-)] = u_l(x_i^-) - \varepsilon s \frac{\partial x_i}{\partial t} \quad (37)$$

$$\rho_{ng}[u_g(x_i^+) - u_g(x_i^-)] = \rho_g D_m \left[\frac{\partial}{\partial x}\frac{\rho_{ng}}{\rho_g}\bigg|_{x_i^+} - \frac{\partial}{\partial x}\frac{\rho_{ng}}{\rho_g}\bigg|_{x_i^-}\right]. \quad (38)$$

4. SOLUTION METHOD

The finite-volume method described in Patankar [20] is used to discretize the equation. The implicit method is used in order to allow for large timesteps. The staggered mesh compatible with application of the conservation principles to each node is used. For $t > t_c$, an adaptive technique was used allowing for the concentration of nodes near the moving interface.

In the funicular regime, the liquid flow dominates. The three differential equations are solved for s, T, and ρ_{ng}. The vapor density is found from $\rho_{cg}(T, p_c)$, i.e. the Clausius–Clapeyron/Kelvin equation [4]. Here, the effect of curvature on ρ_{cg} is not significant until s_{ir} is reached (note that $K \simeq 10^{-11}$ m^2). The results of this implicit technique were checked against those of the explicit technique of ref. [4], and the computed critical time of the two methods agreed to within 3% for a large range of permeabilities.

In the evaporative front regime, the conservation equations in the two domains (dry and wet), and the conditions at the interface of these domains, must be solved simultaneously. In the $x_i \leqslant x \leqslant L$ domain, the unknowns are ρ_{ng}, ρ_{cg}, and T, and the vapor is superheated. The unknowns in the $0 \leqslant x \leqslant x_i$ domain are the same as those given for the funicular regime. In order to start the integration, a small dry region is introduced at $t = t_c$. This was taken small enough so that the results for t, sufficiently larger than Δt, are not influenced by the choice of this initial, imposed dry region. The iteration always begins at $x = L$, and the surface heat and mass balance conditions are solved for T and ρ_{cg}. Then, ρ_{ng} is found from the pressure boundary condition. Next, the nodes in $x_i \leqslant x \leqslant L$ are updated, and the conditions at x_i are

solved. The position of x_i is then computed using $s = s_{ir}$, and by using equation (37). Then, $T(x_i)$ is found from equation (36) and $\rho_{cg}(x_i)$ from $\rho_{cg}[T(x_i), p_c]$, and equation (38) is updated using the new values of T, ρ_{cg}, ρ_{ng} at x_i. This procedure continues until convergence (in terms of overall heat and mass balance) is found according to a prescribed condition (better than 1% in the accumulated heat and mass content of the bed). The standard convergence test of using progressively smaller mesh (and here also by redistribution of the mesh) is performed, and only the results satisfying this test are reported.

Because of the dominance of the liquid flow in the funicular regime, small Δt has to be used in order to avoid instabilities. As $t \to t_c$, the gradient of saturation near the surface increases rapidly, and a high concentration of mesh is used in this region. In the moving front regime, a larger pressure difference develops between $x = x_i$ and L, which also requires small Δt. We have made no special effort to exclude terms that make small contributions nor to devise more efficient solution methods. This area needs further development.

5. RESULTS AND DISCUSSION

The above formulated one-dimensional, transient analysis of both funicular and evaporative front regimes and porosity heterogeneity as well as the results of the experiment outlined in Section 2, are presented below. The results are for $K = 9.9 \times 10^{-12}$ m^2, $\varepsilon = 0.4$, $T_a = 55$°C, $T_0 = 20$°C, $h = 18.3$ W m^{-2} K^{-1}, $s_{ir} = 0.05$, $s_{irg} = 0.02$, and a bed depth of 25.4 mm, for a 0.10 mm glass spheres–ethanol bed.

We chose $a_1 = 0.1$ in equations (23) and (24). Also, because the capillary pressure relation given by equation (31) underestimates the experimental results for p_c and, when used in equations (6) and (29), gives results that do not agree with the experimental observations, we neglected the effect of gravity in the momentum equations. The Leverett reduction, which is based on the experimental results of water–air–nonconsolidated sandstone systems, does not allow for the influence of wettability (ethanol wets the glass spheres fairly well). We note that the formulation given in Section 3 is rather general and, given the required constitutive equations (e.g. p_c, K_l, K_g, D_m, D_h) with sufficient accuracies, accurate predictions can be made using the effect of capillarity, gravity, and thermo-capillarity.

5.1. *Funicular regime*

As was mentioned, the *Bo* and *Re* for the particle size–fluid combination used in the experiment results in constant heat and mass transfer coefficients (i.e. independent of the surface saturation). Figure 3 shows the variation of the mass transfer rate with respect to time. As will be shown, initially the surface temperature drops resulting in the transfer of heat to the surface from both the bed and the ambient. Therefore,

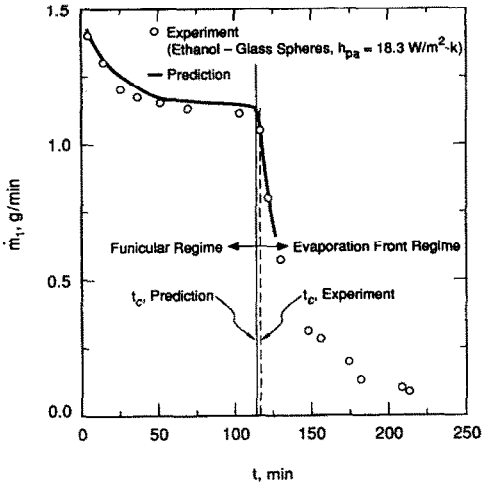

FIG. 3. Variation of mass transfer rate with respect to time. Both the funicular and evaporative front regimes are shown. The experimental results are shown with symbols. The predicted and estimated (using experimental results) critical times are also shown.

larger mass transfer rates occur initially. Later on, the surface temperature rises, and heat begins to flow into the bed resulting in a reduction of the evaporation rate (equation (20)). Note that because of the rather small heat transfer coefficients, the initial transient (bed cooling–heating) occupies a larger portion of the funicular regime period ($0 \leqslant t \leqslant t_c$). Therefore, the so-called constant drying period does not dominate over $0 \leqslant t \leqslant t_c$. For $t > t_c$, the mass transfer rate decreases substantially indicating surface drying. The predicted critical time (the time at which $s = s_{ir}$) and the critical time estimated from the drop in the mass transfer rate and rise in the surface temperature are also marked in Fig. 3. Note that the predicted (114.3 min) and experimental t_c are in very good agreement (this was also found in ref. [4]). The larger scatter existing in the experimental data for small mass transfer is associated with the inaccuracy of measuring small changes in the mass of the bed.

Figure 4 shows the predicted and measured saturation averaged over the entire bed (one-dimensional), and, as expected (because experimental h is used), the agreement is very good. The predicted and measured critical times are also shown, and it is evident that $\partial s/\partial t$ drops significantly for $t > t_c$. Figure 5 shows the predicted and measured surface temperatures, and, as was mentioned, initially the surface temperature drops, and heat flows from the bed to the surface. This is because the bed is not initially at the wet-bulb temperature. As the heat addition from the ambient proceeds, the surface temperature begins to rise, and heat flows into the bed resulting in the preheating of the liquid evaporating on the surface. For $t > t_c$, the surface temperature rises rapidly indicating drying of the surface.

Figure 6 shows the predicted temperature distribution in the bed for various elapsed times. The

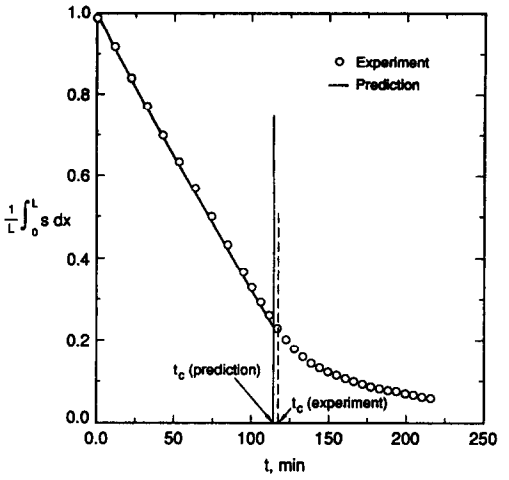

FIG. 4. Predicted and measured variation of the saturation averaged over the bed, during the funicular regime, with respect to time. The critical time is also shown.

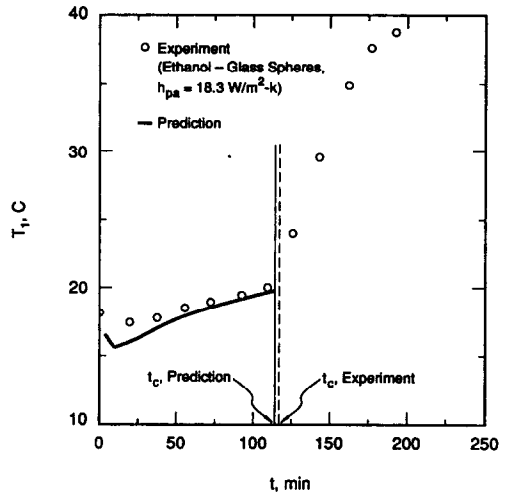

FIG. 5. Predicted and measured variation of the surface temperature with respect to time. The critical time is also shown.

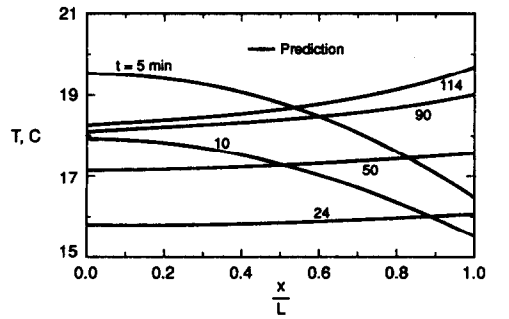

FIG. 6. Predicted temperature distribution for various elapsed times during the funicular regime.

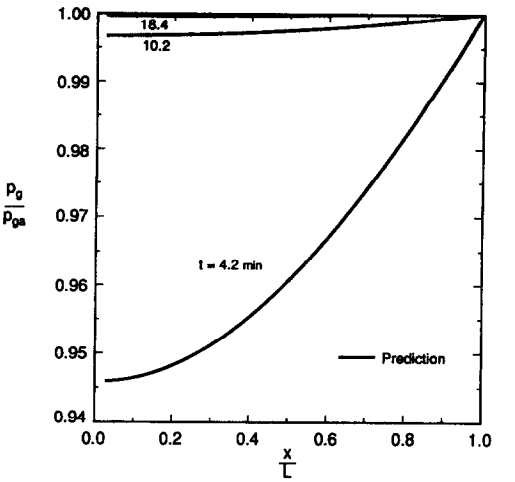

FIG. 7. Predicted gas pressure distribution during early stages of the funicular regime.

initial surface temperature drops, and the consequent heat flow toward the surface (prior to $t = 24$ min) is evident. Note that the presence of the noncondensibles and the resistance to vapor flow causes initial reduction of the pressure (will be shown next) and further decreases in the temperature. Note that as t_c is approached, the bed temperature distribution and the mass transfer rate (Fig. 3) do tend toward asymptotes. Figure 7 shows the predicted total pressure distribution in the bed. The initial total pressure reduction lasts about 20 min. Note that because the vapor and liquid are in thermodynamic equilibrium, in this early stage $\partial p_{cg}/\partial x > 0$, i.e. vapor moves towards the surface. For $t > 20$ min, the vapor moves inward, $\partial p_{cg}/\partial x < 0$. In contrast, the mass averaged velocity given by $\partial p_g/\partial x$ is inward for $t < 20$ min.

The predicted saturation distribution for various elapsed times, prior to $t = t_c$, is shown in Fig. 8. Initially the saturation distribution is nearly uniform.

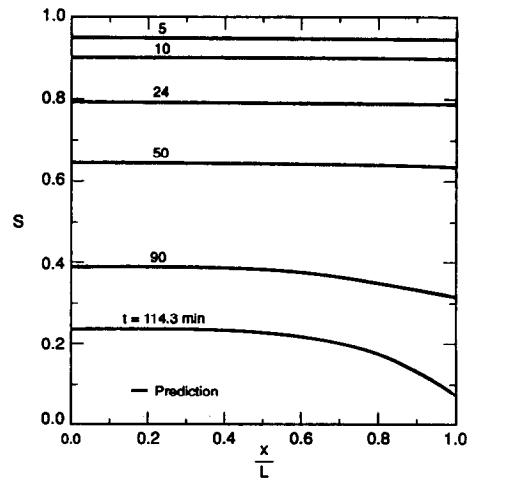

FIG. 8. Distribution of the predicted local saturation during the funicular regime for various elapsed times.

As the saturation decreases and the resistance to the liquid flow increases, the saturation gradient required for capillary pressure driven flow increases until finally the surface saturation, which is the lowest, becomes equal to s_{ir}.

5.2. *Porosity heterogeneity*

Since the critical time depends on the variation of the pressure with respect to saturation, especially for saturations near s_{ir}, we can use the effect of porosity heterogeneity on p_c (Fig. 2) to examine how this heterogeneity influences t_c. We expect that for a given $\bar{\varepsilon}$ and $\Delta\varepsilon$ the critical time would increase as σ_0 increases and $p_c(s \to s_{ir})$ increases. Figure 9 shows the results for $0.0 \leqslant \sigma_0 \leqslant 0.05$, and this increase in t_c is evident. The range of σ_0 is small and perhaps realistic, and is computationally practical. We expect that t_c would increase monotonically for $\sigma_0 \approx 0.20$ (because Fig. 2 shows that $p_c(s \to s_{ir})$ approaches an asymptote) and note that the porosity heterogeneities can be significant. We also note that the empirical results for $p_c(s, \varepsilon, \sigma)$ are generally obtained for beds where ε is locally (within the representative elementary volume) heterogeneous, and, therefore, for more meaningful results, p_c for homogeneous porosity distribution should be used. We expected that for porous media (not restricted to packed beds) where the average pore size d is small, $\Delta\varepsilon \approx \bar{\varepsilon}$, and these small pores ($\varepsilon \to 0$) are connected, even at low saturations ($s \to s_{ir}$), the surface will not dryout, and t_c extends until almost the entire bed is at $s \approx s_{ir}$.

5.3. *Moving evaporative front regime*

The predicted mass transfer rate for $t > t_c$ was included in Fig. 3 along with that for the funicular regime. The significant drop in $\dot{m}$, which is the result of resistance to heat and mass transfer, in the dry region, is evident in this figure. The predicted and measured mass transfer rates are in very good agreement. The computation is not continued as far as the available experimental data because of the intensive computation resulting from the inclusion of both dry and wet regions and because of the inclusion of all the terms in the conservation equations. However, the suitability of the formulation of the evaporation front regime given in Section 3.3 for prediction of mass transfer rate is evident.

Figure 10 shows the predicted temperature distribution for several elapsed times (passed the critical time) along with some experimental results. The formulation slightly overpredicts the surface temperature. The position of the evaporation front x_i is also shown. Note that the predicted critical time is used and because of the slight difference between this and the experimental results (which is larger than 1 min), the results for $t = t_c + 1$ min are not expected to be in good agreement with the experiments. Figure 11 shows the predicted distribution of the total pressure for the same elapsed times as in Fig. 10. Note that vapor flows from the evaporative front to the surface thus requiring $\partial p_{cg}/\partial x < 0$. The results of Fig. 11 show that $\partial p_g/\partial x$ is also negative in $x_i \leqslant x \leqslant L$. Thus the mass velocity u_g is positive (moving away from the evaporative front toward the surface). The vapor is superheated in the dry region (temperature distribution in the dry region is shown in Fig. 10) and in equilibrium with the liquid in the wet region. As the elapsed time increases, the total pressure in the wet region increases indicating significant bulk evap-

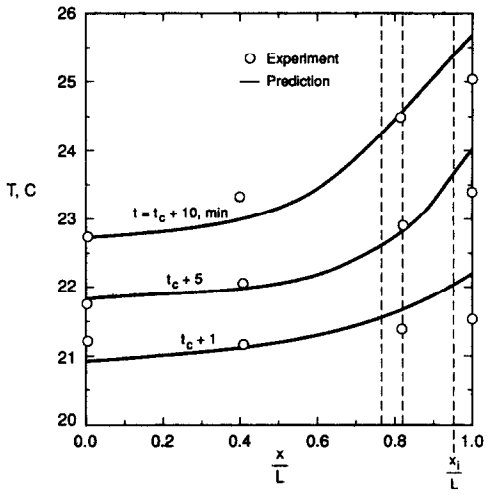

FIG. 10. Measured and predicted temperature distributions during the early stages of the evaporative front regime.

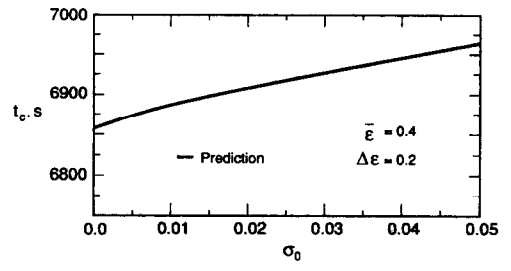

FIG. 9. Variation of the predicted critical time with respect to the standard deviation in the Gaussian distribution of the porosity heterogeneity.

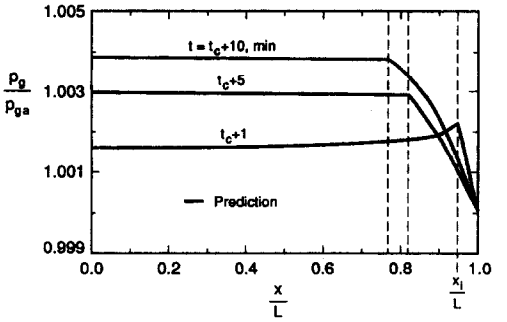

FIG. 11. Distribution of the predicted gas pressure during early stages of the evaporative front regime.

oration ($\dot{n}$ in equation (15)), as a consequence of a rise in the temperature of the wet region (Fig. 10).

6. CONCLUSIONS

Heat addition to a partially saturated porous medium that is everywhere below the boiling point is examined through the funicular regime ($s(x) > s_{ir}$) and the moving front regime. The effect of temperature nonuniformity and the consequent surface tension nonuniformity on the liquid and gas phase flows is examined, and the appropriate momentum equations are presented. The critical time (time at which $s(x = L) = s_l = s_{ir}$) can be readily determined from the integration of these and other related conservation equations. Since the capillary pressure–saturation relation determines the critical time, the effect of absolute permeability heterogeneities on the capillary pressure and the critical time is examined. The results show that the porosity heterogeneities, with normal distributions, increase the critical time. The speed of the evaporation front and the instantaneous mass transfer rate during this regime, are also predicted. The predicted results are in good agreement with the experiments performed using a glass spheres–ethanol bed.

REFERENCES

1. S. J. Gregg and K. S. W. Sing, *Adsorption, Surface Area and Porosity*. Academic Press, New York (1982).
2. R. Defay and I. Prigogine, *Surface Tension and Adsorption*. Wiley, New York (1966).
3. F. A. L. Dullien, *Porous Media: Fluid Transport and Pore Structure*. Academic Press, New York (1979).
4. M. Kaviany and M. Mittal, Funicular state in drying of a porous slab, *Int. J. Heat Mass Transfer* **30**, 1407–1418 (1987).
5. S. Whitaker and W. T.-H. Chou, Drying granular porous media—theory and experiment, *Drying Technol.* **1**, 3–33 (1983).
6. M. A. Stanish, G. S. Schajer and F. Kayihan, A mathematical model of drying for hygroscopic porous media, *A.I.Ch.E. Jl* **32**, 1301–1311 (1986).
7. M. Greiner and R. F. Winter, Forced flow evaporation at high mass transfer rates, *Ger. Chem. Engng* **1**, 352–360 (1978).
8. S. Whitaker, Flow in porous media II: the governing equations for immiscible, two-phase flow, *Transp. Porous Media* **1**, 105–125 (1986).
9. J. Bear and J. Bensabat, Advective fluxes in multiphase porous media under non-isothermal conditions, *Transp. Porous Media* **4**, 423–448 (1989).
10. G. H. Neale and W. K. Nader, Prediction of transport process within homogeneous swarm of spherical spheres, *A.I.Ch.E. Jl* **19**, 112–119 (1973).
11. D. L. Koch and J. Brady, Dispersion in fixed beds, *J. Fluid Mech.* **154**, 399–427 (1985).
12. W. H. Somerton, J. A. Keese and S. C. Chu, Thermal behavior of unconsolidated oil sands, *SPE J.* **14**, 513–521 (1974).
13. K. S. Udell and J. S. Fitch, Heat and mass transfer in capillary porous media considering evaporation, condensation and non-condensible gas effects. In *Heat Transfer in Porous Media and Particulate Flows*, ASME HTD-Vol. 46, pp. 163–210 (1985).
14. R. Krupiczka, Analysis of thermal conductivity in granular materials, *Int. Chem. Engng* **7**, 122–144 (1967).
15. J. A. Rogers and M. Kaviany, Variation of heat and mass transfer coefficients during drying of granular-beds, *J. Heat Transfer* **112**, 668–674 (1990).
16. Y.-X. Tao and M. Kaviany, Simultaneous heat and mass transfer from a two-dimensional, partially liquid covered surface, *J. Heat Transfer* **113**, 875–882 (1991).
17. E.-U. Schlünder, On the mechanism of the constant drying rate period and its relevance to diffusion controlled catalytic gas phase reactions, *Chem. Engng Sci.* **43**, 2685–2688 (1988).
18. M. Kaviany, *Principles of Heat Transfer in Porous Media*. Springer, New York (1991).
19. M. C. Leverett, Capillary behavior in porous media, *Trans. AIME* **142**, 152–169 (1941).
20. S. Patankar, *Numerical Heat Transfer and Fluid Flow*. McGraw-Hill, New York (1980).

REGIMES FUNICULAIRE ET DE FRONT EVAPORATIF DANS LE SECHAGE CONVECTIF DES LITS GRANULAIRES

Résumé—Le chauffage convectif d'un lit fixe partiellement saturé et les évaporations de surface et interne sont considérés dans les cas où la température partout dans le lit est au dessous de la température de saturation à la pression locale. Dans la première période où la phase liquide est continue (régime funiculaire), on examine l'effet de la non uniformité de tension superficielle du liquide et des écoulements de la phase gazeuse. Le temps critique (le temps au bout duquel la saturation de la surface devient égale à la saturation immobile) est trouvé par intégration des équations de bilan. On examine l'effet des hétérogénéités de la perméabilité absolue sur ce temps critique et on montre que, pour des distributions normales de porosité, le temps critique croît plus que pour des perméabilités homogènes. Le transfert de masse pendant le régime de front évaporatif est prédit en traitant à la fois les régions sèche et humide et l'interface mobile. On conduit une expérimentation dans laquelle un lit de billes de verre 0,10 mm-éthanol est séché par convection et un bon accord est trouvé entre les flux de masse prédits et calculés, entre les temps critiques et entre les températures de surface.

BEREICHE DES KAPILLARTRANSPORTS UND DER VERDAMPFUNGSFRONT BEI DER KONVEKTIVEN TROCKNUNG VON SCHÜTTUNGEN

Zusammenfassung—Es wird die konvektive Beheizung einer anfangs teilweise gesättigten Schüttung und die sich ergebende Verdampfung von Flüssigkeit an der Oberfläche und im Inneren betrachtet. Dabei ist die Temperatur im Schüttbett überall unterhalb der Sättigungstemperatur bei dem jeweiligen örtlichen Gesamtdruck. In einem ersten Zeitraum, wo die Flüssigkeit die kontinuierliche Phase darstellt (Bereich des Kapillartransports), wird der Einfluß der ungleichmäßigen Oberflächenspannung auf die Strömung von flüssiger und gasförmiger Phase untersucht. Durch Integration der Erhaltungsgleichungen ergibt sich der kritische Zeitpunkt, der dadurch gekennzeichnet ist, daß die Oberflächensättigung den Wert der stationären Sättigung erreicht. Der Einfluß der Heterogenität der absoluten Permeabilität auf diese kritische Zeit wird untersucht. Dabei zeigt sich, daß für normale Porositätsverteilungen die kritische Zeit größer ist als bei homogenen Permeabilitäten. Der Stofftansport im Bereich der Verdampfungsfront wird unter Berücksichtigung des trockenen und des feuchten Bereichs sowie der beweglichen Grenzfläche ebenfalls berechnet. In einem ergänzenden Versuch wird eine Schüttung aus 0,10 mm Glaskügelchen mit Ethanol konvektiv getrocknet. Die gemessenen und berechneten Werte für den Stofftransport, die kritische Zeit und die Oberflächentemperatur stimmen gut überein.

КАНАТНЫЙ И ИСПАРИТЕЛЬНЫЙ РЕЖИМЫ ДВИЖЕНИЯ ФРОНТА ИСПАРЕНИЯ ПРИ КОНВЕКТИВНОЙ СУШКЕ ГРАНУЛИРОВАННЫХ СЛОЕВ МАТЕРИАЛА

Аннотация—Исследуются конвективный нагрев первоначально частично насыщенных жидкостью плотных слоев и последующее ее испарение с поверхности изнутри слоя в случаях, когда температура во всем слое ниже температуры насыщения при локальном суммарном давлении. В первом периоде существования сплошной жидкой фазы (канатный режим) анализируется влияние неоднородности поверхностного натяжения на течение в жидкой и газообразной фазах. Критическое время (при котором насыщение поверхности становится равным насыщению неподвижной жидкостью) определяется интегрированием уравнений сохранения. Оценивается влияние неоднородностей абсолютной проницаемости на критическое время и показано, что при нормальном распределении порозности критическое время возрастает по сравнению со случаем однородных проницаемостей. Определяется также скорость массопереноса в режиме движения фронта испарения на основе анализа сухого и влажного участков, а также движущейся границы раздела. Проводился эксперимент, при котором осуществлялась конвективная сушка слоя, состоящего из стеклянных шариков диаметром 0,10 мм и этанола, и получено хорошее согласие между теоретическими и экспериментальными результатами для скорости массопереноса, критического времени и температуры поверхности.